

Single-Collision Model for Non-Line-of-Sight UV Communication Channel With Obstacle

Tianfeng Wu[†], Fang Yang[†], Renzhi Yuan[‡], Tian Cao[§], Ling Cheng^{*}, Jian Song^{†,‡}, Julian Cheng^{*}, and Zhu Han[⊕]

[†]Department of Electronic Engineering, BNRist, Tsinghua University, Beijing 100084, P. R. China

[‡]State Key Laboratory of Networking and Switching Technology,

Beijing University of Posts and Telecommunications, Beijing, 100876, P. R. China

[§]School of Telecommunications Engineering, Xidian University, Xi'an 710071, P. R. China

^{*}School of Electrical and Information Engineering, University of the Witwatersrand, Johannesburg 2000, South Africa

[‡]Shenzhen International Graduate School, Tsinghua University, Shenzhen 518055, P. R. China

^{*}School of Engineering, The University of British Columbia, Kelowna, BC, V1V 1V7, Canada

[⊕]Department of Electrical and Computer Engineering, University of Houston, Houston, TX 77004 USA

Email: wtf22@mails.tsinghua.edu.cn, fangyang@tsinghua.edu.cn, renzhi.yuan@bupt.edu.cn, caotian@xidian.edu.cn,

ling.cheng@wits.ac.za, jsong@tsinghua.edu.cn, julian.cheng@ubc.ca, hanzhu22@gmail.com

Abstract—Existing research on non-line-of-sight (NLoS) ultraviolet (UV) channel modeling mainly focuses on scenarios where the signal propagation process is not affected by any obstacle and the radiation intensity (RI) of the light source is uniformly distributed. To eliminate these restrictions, we propose a single-collision model for the NLoS UV channel incorporating a cuboid-shaped obstacle, where the RI of the UV light source is modeled as the Lambertian distribution. For easy interpretation, we categorize the intersection circumstances between the receiver field-of-view and the obstacle into six cases and provide derivations of the weighting factor for each case. To investigate the accuracy of the proposed model, we compare it with the associated Monte Carlo photon tracing model via simulations and experiments. Results verify the correctness of the proposed model. This work reveals that obstacle avoidance is not always beneficial for NLoS UV communications and provides guidelines for relevant system design.

Index Terms—Lambertian distribution, obstacle, scattering and reflection, NLoS UV communications.

I. INTRODUCTION

CURRENTLY, radio frequency (RF) technology is broadly employed in wireless communication networks thanks to its attractive advantages such as low cost, easy deployment, and high penetration ability [1]. However, this technology also faces certain challenges, for example, spectrum scarcity, electromagnetic interference (EMI), and communication security [2], [3]. To address these problems, alternative technologies including millimeter-wave (mm-Wave), terahertz (THz) [4], infrared (IR), visible light communications (VLC), and ultraviolet (UV) communications [5] are introduced to existing wireless networks. Compared to RF, UV possesses the advantages of huge bandwidth without licensing and immunity to EMI [6]. In comparison with mm-Wave, THz, IR, and VLC, which primarily support line-of-sight (LoS) transmission, UV can transmit information via non-line-of-sight (NLoS) links, namely, atmospheric scattering [7]. Moreover, the background noise of UV communication systems adopting 200-280 nm bands can be ignored [8]. Motivated by these intriguing benefits,

UV communication technology has great potential to guarantee future ubiquitous communications by integrating with other wireless communication technologies.

To date, research directed at UV communications has focused on several aspects: light sources and detectors, channel modeling, modulation and coding, networking, and performance improvement techniques [2], [3]. Among these studies, channel modeling is predominantly investigated, which includes single-scattering model [9], multiple-scattering model [10], turbulence channel model [11], empirical path loss model [12], and related simplified channel models [13]–[16]. These models play a crucial role in the performance evaluation of NLoS channels, such as channel attenuation and delay spread, and meanwhile provide guidelines for the related system design. However, the existing NLoS channel models primarily focus on scenarios where signal links are not affected by any obstacle [17], and the radiation intensity (RI) of the UV light source is uniformly distributed [18]. Exactly, when the obstacle appears in the overlap volume between the transceiver field-of-views (FoVs) and the RI of the UV light source is non-uniformly distributed, existing models suffer from reduced accuracy in predicting system performance.

To tackle the aforementioned problems, we propose a channel model for NLoS UV communications considering an obstacle, where the RI of the light source is modeled as the Lambertian distribution based on the existing research that has been verified by outdoor measurements [18], [19]. Moreover, the shape of the obstacle is modeled as a cuboid, which is consistent with the shape of most buildings in urban areas [17]. Furthermore, relevant numerical results and experiments are provided to verify the correctness of the proposed model. Compared to related works, which assume that the reflective surface [18] or the obstacle thickness [17] is infinitely large and adopt the Monte Carlo photon tracing (MCPT) method for modeling, the proposed model takes the obstacle's coordinates, thickness,

width, and height into consideration, and utilizes the integration method for modeling.

Notations: Throughout this paper, boldface lowercase letters (e.g. ν) and boldface uppercase letter pairs (e.g. \mathbf{RN}) represent vectors, and $\|\cdot\|$ denotes the Euclidean norm of a vector.

II. SYSTEM MODEL

As shown in Fig. 1, the transceiver parameters are defined as follows: β_r represents the half-FoV angle of the receiver (R); ϑ_t denotes the transmitter (T) elevation angle, which is positive if rotating clockwise from the projection of the beam axis on the plane XRY; ϑ_r represents the receiver elevation angle, which is positive if rotating anticlockwise from \mathbf{RO}' , where \mathbf{RO}' denotes the projection of the FoV axis \mathbf{RO} (O is an arbitrary point on the FoV axis other than R) on the plane XRY, O' is the projection of the point O on the XRY, and this representation also applies to other points such as obstacle vertices; α_t and α_r are the azimuth angles of T and R, respectively, which are positive if rotating anticlockwise from X positive axis; ε and ν represent the distances from the scattering point P (or the reflective area) to T and R, respectively; \mathcal{A} is the detection area of the receiver aperture; r represents the communication range; and P_t denotes the transmitted power.

Regarding the cuboid-shaped obstacle, w and s represent the obstacle's width and thickness, respectively, and z_m denotes the height of the obstacle above the plane XRY. Owing to the symmetry, x_m and y_m coordinates of the obstacle's central point M are set to $(-\infty, -s/2)$ and $(w/2, r - w/2)$, respectively. Thus, X and Y coordinates of the obstacle vertices A, B, C, and D can be expressed as

$$\mathbf{A, B, C, D} : \begin{cases} x_a = x_b = x_m - s/2, \\ x_c = x_d = x_m + s/2, \\ y_a = y_d = y_m + w/2, \\ y_b = y_c = y_m - w/2, \\ z_a = z_b = z_c = z_d = z_m. \end{cases} \quad (1)$$

For the light-emitting diode (LED)-based UV light source, its RI is modeled as the generalized Lambertian distribution [18], and can be given by

$$\mathcal{L}(\varpi) = \begin{cases} \frac{(\kappa + 1) \cos^\kappa \varpi}{2\pi}, & 0 \leq \varpi \leq \pi/2, \\ 0, & \pi/2 < \varpi \leq \pi, \end{cases} \quad (2)$$

where ϖ represents the angle between the transmitter's pointing direction and the photon's emitting direction, and κ denotes the order of Lambertian emission, which can be expressed as $\kappa = -\ln 2 / \ln \cos(\beta_{1/2}/2)$ and $\beta_{1/2}$ denotes the full-width at half-illuminance of the LED.

III. DERIVATION OF SCATTERED ENERGY

Consider an impulse of energy Q_t transmitted over the whole beam into a homogeneous scattering and absorbing medium. If P lies inside the overlap volume between the transmitter beam and the receiver FoV, the unextinguished energy arriving at the

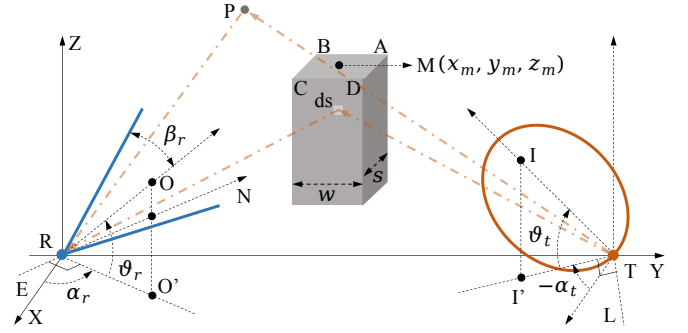


Fig. 1. Illustration of NLoS UV channel containing a cuboid-shaped obstacle.

differential volume dv will be scattered. Referring to [7], dv can be considered as a secondary source with an energy as

$$dQ_{\text{sca}} = Q_t \mathcal{L}(\varpi) \exp(-k_e \varepsilon) k_s \varepsilon^{-2} \mathcal{S}_{\text{wei}, \varepsilon} dv, \quad (3)$$

where $\mathcal{S}_{\text{wei}, \varepsilon}$ denotes the transmitter weighting factor, which is utilized to determine whether the emitting ray is blocked by the obstacle. k_e is the atmospheric extinction coefficient, which can be obtained by the addition of the scattering coefficient k_s and the absorption coefficient k_a .

On this basis, the received energy contributed by dv can be derived as

$$dQ_{r, \text{sca}} = dQ_{\text{sca}} P(\cos \beta) \frac{\mathcal{A} \cos \delta}{\nu^2} \exp(-k_e \nu) \mathcal{S}_{\text{wei}, \nu}, \quad (4)$$

where $\mathcal{S}_{\text{wei}, \nu}$ represents the receiver weighting factor, which is employed to determine whether the receiving ray is blocked by the obstacle; β and δ denote the angles between the vectors \mathbf{TP} and \mathbf{RP} , and \mathbf{RP} and \mathbf{RO} , respectively; and $P(\cos \vartheta)$ represents the scattering phase function [8].

Substituting (1) and (2) into (3) and integrating $dQ_{r, \text{sca}}$ over the whole overlap volume, we can obtain

$$Q_{r, \text{sca}} = \int_{\vartheta_{\min}}^{\vartheta_{\max}} \int_{\psi_{\min}}^{\psi_{\max}} \int_{\nu_{\min}}^{\nu_{\max}} Q_t k_s \mathcal{A} \mathcal{F} \mathcal{S}_{\text{wei}} d\nu d\psi d\vartheta, \quad (5)$$

where

$$\mathcal{F} = \frac{\kappa + 1}{2\pi \varepsilon^2} \cos^\kappa \varpi P(\cos \beta) \cos \delta \exp[-k_e(\varepsilon + \nu)] \cos \psi. \quad (6)$$

Here, ψ denotes the angle between the vectors \mathbf{RN} and \mathbf{RS} (\mathbf{RS} is located on the plane \mathcal{N}_ϑ and enclosed by the receiver FoV), which is positive when rotating anticlockwise from \mathbf{RN} . \mathcal{N}_ϑ represents the plane passing through \mathbf{RN} and is perpendicular to the plane \mathbf{ROO}' , which rotates around the line \mathbf{RE} , where \mathbf{RE} is located on the plane \mathbf{XRY} and perpendicular to the line \mathbf{RO}' , and the subscript ϑ denotes the angle between the vectors \mathbf{RO} and \mathbf{RN} , which is positive if taken anticlockwise from \mathbf{RO} . For \mathcal{S}_{wei} , it is the total weighting factor and can be given by $\mathcal{S}_{\text{wei}} = \mathcal{S}_{\text{wei}, \varepsilon} \mathcal{S}_{\text{wei}, \nu}$. In the following, the unspecified quantities in (5), ϑ_{\min} , ϑ_{\max} , ψ_{\min} , ψ_{\max} , ν_{\min} , ν_{\max} , and \mathcal{S}_{wei} , will be derived combined with specific circumstances.

Considering the wide coverage area of light sources based on Lambertian distribution, the upper and lower limits of the triple integral in (5) are determined by the receiver conical surface.

As regards ϑ_{\min} and ϑ_{\max} , they can be given by $-\beta_r$ and β_r , respectively, and $\phi_{\max} = \vartheta_r + \vartheta_{\max}$ is assumed to be less than $\pi/2$. Regarding ψ_{\min} and ψ_{\max} , they can be derived as

$$\psi_{\min} = -\arctan\left(\frac{\sqrt{\tan^2 \beta_r - \tan^2 \vartheta}}{\sec \vartheta}\right), \quad (7a)$$

$$\psi_{\max} = \arctan\left(\frac{\sqrt{\tan^2 \beta_r - \tan^2 \vartheta}}{\sec \vartheta}\right). \quad (7b)$$

For ν_{\min} and ν_{\max} , they are set to 0 and $+\infty$, respectively, and at the same time a constraint needs to be imposed, which can be expressed as

$$\frac{1}{\varepsilon} \boldsymbol{\varepsilon}^T \boldsymbol{\mu} \geq \cos \frac{\pi}{2}, \text{ i.e., } \boldsymbol{\varepsilon}^T \boldsymbol{\mu} \geq 0, \quad (8)$$

where $\boldsymbol{\mu} = [\cos \vartheta_t \cos \alpha_t, \cos \vartheta_t \sin \alpha_t, \sin \vartheta_t]^T$ and $\boldsymbol{\varepsilon} = [x, y - r, z]^T$. The coordinates of the point P can be expressed as

$$\text{P} : \begin{cases} x = \nu \cos \psi \cos \phi \cos(\alpha_r + \omega) \sec \omega, \\ y = \nu \cos \psi \cos \phi \sin(\alpha_r + \omega) \sec \omega, \\ z = \nu \cos \psi \sin \phi, \end{cases} \quad (9)$$

where $\phi = \vartheta_r + \vartheta$ and $\omega = \arctan(\tan \psi / \cos \phi)$. Following that, the value of \mathcal{S}_{wei} is investigated for different cases.

Since the receiver parameters (i.e., α_r , ϑ_r , and β_r), obstacle parameters (i.e., w , s , x_m , y_m , and z_m) and the communication range r are variable, the intersection circumstances between the receiver FoV and the obstacle are very complicated. To address the modeling problems of all possible scenarios, we choose the most representative scenario for modeling, where \mathcal{N}_ϑ intersects with obstacle vertices in the order A, D, B, and C when rotating anticlockwise from the plane $\mathcal{N}_{-\vartheta_r}$, $\phi_{\max} > \Sigma_c$, and $\phi_{\min} = \vartheta_r + \vartheta_{\min} < \Sigma_a$. Based on the geometric relationships, Σ_u can be derived as

$$\Sigma_u = \arctan\left(\frac{z_m \sqrt{\cot^2 \alpha_r + 1}}{|x_u \cot \alpha_r + y_u|}\right), \quad (10)$$

where the subscript u can be a , b , c , and d . Next, we first solve for the value of \mathcal{S}_{wei} corresponding to the interval $\vartheta \in (-\beta_r, \Sigma_a - \vartheta_r]$. In this situation, the intersection circumstances between the plane \mathcal{N}_ϑ and the obstacle can be summarized into six cases, and each case will be investigated detailedly on the condition that (8) holds. Throughout the entire derivation process, α_t and α_r are set to $(-\pi, -\pi/2)$ and $(\pi/2, \pi)$, respectively, and $\phi_{\min} = \vartheta_r + \vartheta_{\min}$ is assumed to be larger than $-\pi/2$.

Case 1: $\Psi_{\max} > \Psi_{\min} \geq \Phi_{\max} > \Phi_{\min}$

First, the parameters Φ_{\max} , Φ_{\min} , Ψ_{\max} , and Ψ_{\min} need to be specified. For Φ_{\max} and Φ_{\min} , they can be derived as

$$\Phi_{\min} = \alpha_r + \psi_{\min} - \pi/2, \quad (11a)$$

$$\Phi_{\max} = \alpha_r + \psi_{\max} - \pi/2, \quad (11b)$$

while for Ψ_{\max} and Ψ_{\min} , they can be expressed as $\Psi_{bb'}$ and $\Psi_{dd'}$, respectively. $\Psi_{uu'}$ denotes the angle between the vectors $\mathbf{RP}_{uu'}$ and \mathbf{RK} , where $P_{uu'}$ represents the intersection point of the plane \mathcal{N}_ϑ with the line UU' (e.g., $P_{bb'}$ and the line BB')

and \mathbf{RK} represents the intersection ray between the planes YRZ and \mathcal{N}_ϑ . After algebraic operations, $\Psi_{uu'}$ can be expressed as

$$\Psi_{uu'} = \arccos\left(\frac{y_{uu'} \mathcal{G}_3 - z_{uu'} \mathcal{G}_2}{\sqrt{\mathcal{G}_2^2 + \mathcal{G}_3^2} \|\mathbf{RP}_{uu'}\|}\right), \quad (12)$$

where $z_{uu'} = -(\mathcal{G}_1 x_u + \mathcal{G}_2 y_u) / \mathcal{G}_3$, and \mathcal{G}_1 , \mathcal{G}_2 , and \mathcal{G}_3 can be derived as

$$\mathcal{G}_1 = -\cos \alpha_r \sec^2 \vartheta \sin(2\phi) \tan \theta, \quad (13a)$$

$$\mathcal{G}_2 = -\sin \alpha_r \sec^2 \vartheta \sin(2\phi) \tan \theta, \quad (13b)$$

$$\mathcal{G}_3 = 2 \sec^2 \vartheta \cos^2 \phi \tan \theta. \quad (13c)$$

Here, $\theta = \arctan[\sec \phi (\tan^2 \beta_r - \tan^2 \vartheta)^{1/2} \cos \vartheta]$. In this case, \mathcal{S}_{wei} is equal to 1.

Case 2: $\Phi_{\max} > \Phi_{\min} \geq \Psi_{\max} > \Psi_{\min}$

Before deriving the value of \mathcal{S}_{wei} , the parameters σ and Υ_t need to be specified. As illustrated in Fig. 1, the plane \mathcal{C}_σ is perpendicular to the plane TII' , which rotates around the line TL , and the subscript σ is the angle between the planes LTI' and \mathcal{C}_σ , which is positive if rotating clockwise from LTI' . After algebraic operations, σ can be expressed as

$$\sigma = \begin{cases} \Theta, & \cot \alpha_t x + y < r, \\ \pi/2, & \cot \alpha_t x + y = r, \\ \pi - \Theta, & \cot \alpha_t x + y > r, \end{cases} \quad (14)$$

where $\Theta = \arctan(z \sqrt{1 + \cot^2 \alpha_t} / |x \cot \alpha_t + y - r|)$. Then, we assume that \mathcal{C}_σ intersects with obstacle vertices in the order B, C, A, and D when rotating clockwise from the plane \mathcal{C}_0 , and the corresponding σ values are σ_b , σ_c , σ_a , and σ_d , respectively, which can be determined through (14). Υ_t represents the angle between the vectors \mathbf{TP} and \mathbf{TG} , where TG is the intersection ray between YRZ and \mathcal{C}_σ , and Υ_{uj} denotes the angle between the vectors \mathbf{TF}_{uj} and \mathbf{TG} , where F_{uj} is the intersection point of \mathcal{C}_σ with the line UJ (e.g., F_{ad} and the line AD). Based on the geometric relationships, Υ_{uj} can be expressed as

$$\Upsilon_{uj} = \cos^{-1}\left(\frac{\cos \sigma y_{uj} + \sin \alpha_t \sin \sigma z_{uj} - r \cos \sigma}{\sqrt{\sin^2 \alpha_t \sin^2 \sigma + \cos^2 \sigma} \|\mathbf{TF}_{uj}\|}\right), \quad (15)$$

where the equation of \mathcal{C}_σ can be derived as

$$\sin \sigma [\cos \alpha_t x + \sin \alpha_t (y - r)] - \cos \sigma z = 0. \quad (16)$$

Following that, the values of Υ_{\max} and Υ_{\min} are investigated. If $\sigma \leq \sigma_c$, $\Upsilon_{\max} = \Upsilon_{aa'}$ and $\Upsilon_{\min} = \Upsilon_{cc'}$, while if $\sigma_c < \sigma \leq \sigma_a$, the value of Υ_{\min} is changed to Υ_{cd} , and if $\sigma_a < \sigma < \sigma_d$, the value of Υ_{\max} is modified to Υ_{ad} .

In this case, if $\sigma \geq \sigma_d$, \mathcal{S}_{wei} is equal to 1, while if $\sigma < \sigma_d$, we choose the circumstance where $\sigma \leq \sigma_b$ as an example to derive the value of \mathcal{S}_{wei} . Specifically, $\mathcal{S}_{\text{wei}} = 1$ when $\Upsilon_t > \Upsilon_{\max}$, or $\Upsilon_t < \Upsilon_{\min}$. This analysis process also applies to the remaining four cases.

Case 3: $\Phi_{\max} > \Psi_{\max} > \Phi_{\min} \geq \Psi_{\min}$

In the situation where $\Phi_{\min} \geq \Psi_{cc'}$, the value of \mathcal{S}_{wei} equal to 1 contains two scenarios: i) $\Upsilon_t < \Upsilon_{\min}$; and ii) $\Upsilon_t > \Upsilon_{\max}$

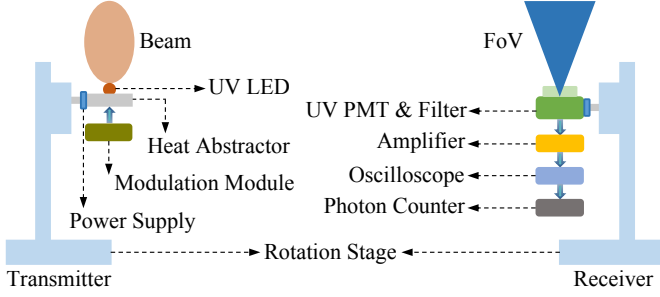


Fig. 2. Schematic diagram of NLoS UV communication systems.

and $\Upsilon_r \in (\Psi_{\max}, \Phi_{\max}]$, where Υ_r denotes the angle between the vectors \mathbf{RP} and \mathbf{RK} .

In the situation where $\Phi_{\min} < \Psi_{cc'}$, the value of \mathcal{S}_{wei} equal to 1 contains three scenarios: i) $\Upsilon_r \in [\Phi_{\min}, \Psi_{cc'}]^\supset$, where \supset is the distance constraint imposed on ν and can be given by

$$\supset : \nu < \frac{\|\mathbf{RP}_{dd'}\| \sin \Lambda_{dd'}}{\sin(\Upsilon_r - \Psi_{dd'} + \Lambda_{dd'})}, \quad (17)$$

and $\Lambda_{dd'}$ denotes the angle between the vectors $\mathbf{P}_{cc'}\mathbf{P}_{dd'}$ and $\mathbf{RP}_{dd'}$; ii) $\Upsilon_r \in (\Psi_{cc'}, \Phi_{\max}]$ and $\Upsilon_t < \Upsilon_{\min}$; and iii) $\Upsilon_r \in (\Psi_{\max}, \Phi_{\max}]$ and $\Upsilon_t > \Upsilon_{\max}$.

Case 4: $\Phi_{\max} > \Psi_{\max} > \Psi_{\min} \geq \Phi_{\min}$

In this case, the value of \mathcal{S}_{wei} equal to 1 contains three scenarios: i) $\Upsilon_r \in [\Phi_{\min}, \Psi_{\min}] \cup [\Psi_{\min}, \Psi_{cc'}]^\supset$; and the rest two scenarios are consistent with the second and third scenarios in **Case 3** where $\Phi_{\min} < \Psi_{cc'}$.

Case 5: $\Psi_{\max} \geq \Phi_{\max} > \Phi_{\min} \geq \Psi_{\min}$

In the situation where $\Phi_{\max} \leq \Psi_{cc'}$, \mathcal{S}_{wei} is equal to 1 when $\Upsilon_r \in [\Phi_{\min}, \Phi_{\max}]^\supset$, while in the situation where $\Phi_{\min} \geq \Psi_{cc'}$, \mathcal{S}_{wei} is equal to 1 when $\Upsilon_t < \Upsilon_{\min}$, and in the situation where $\Phi_{\min} < \Psi_{cc'}$ and $\Phi_{\max} > \Psi_{cc'}$, scenarios for the circumstance where $\mathcal{S}_{\text{wei}} = 1$ are the same as the first and second scenarios in **Case 3** where $\Phi_{\min} < \Psi_{cc'}$.

Case 6: $\Psi_{\max} \geq \Phi_{\max} > \Psi_{\min} > \Phi_{\min}$

In the situation where $\Phi_{\max} \leq \Psi_{cc'}$, \mathcal{S}_{wei} is equal to 1 when $\Upsilon_r \in [\Phi_{\min}, \Psi_{\min}] \cup [\Psi_{\min}, \Phi_{\max}]^\supset$, and in the situation where $\Phi_{\max} > \Psi_{cc'}$, the value of \mathcal{S}_{wei} equal to 1 has two scenarios. The first scenario is consistent with the counterpart in **Case 4**, and the second scenario is in accordance with the counterpart in **Case 3** where $\Phi_{\min} < \Psi_{cc'}$.

As for the ϑ intervals $(\Sigma_a - \vartheta_r, \Sigma_d - \vartheta_r]$, $(\Sigma_d - \vartheta_r, \Sigma_b - \vartheta_r]$, and $(\Sigma_b - \vartheta_r, \Sigma_c - \vartheta_r]$, the derivation of \mathcal{S}_{wei} is in accordance with that of the interval $(-\beta_r, \Sigma_a - \vartheta_r]$, and therefore is not repeated. Regarding the equation of \mathcal{N}_ϑ , it can be expressed as $\mathcal{G}_1 x + \mathcal{G}_2 y + \mathcal{G}_3 z = 0$. When $\vartheta \geq \Sigma_c - \vartheta_r$, the value of \mathcal{S}_{wei} is equal to 1 on the conditions that (8) holds and the obstacle does not block the photon's emitting link. Regarding the energy contribution of the special ray Γ , which is the intersection ray between the receiver FoV and the plane $\mathcal{N}_{-\beta_r}$, it can also be determined referring to the derivation process of the ϑ interval $(-\beta_r, \Sigma_a - \vartheta_r]$. This is because Γ intersects with an obstacle is a special situation of the situations where the cross-section of the receiver FoV intersects with an obstacle.

IV. DERIVATION OF REFLECTED ENERGY

Based on the above derivation, we can obtain the contribution of atmospheric scattering $\mathcal{Q}_{r,\text{sca}}$ to the total received energy \mathcal{Q}_r . In the following, the contribution of obstacle reflection $\mathcal{Q}_{r,\text{ref}}$ to \mathcal{Q}_r will also be investigated.

From Fig. 1, it can be found that the effective reflection area (ERA) is located on the surface CDD'C' and can be given by

$$\text{ERA} : \begin{cases} x = x_m + s/2, \\ y \in [y_m - w/2, y_m + w/2], \\ \mathcal{G}_1 x + \mathcal{G}_2 y + \mathcal{G}_3 z \leq 0, \phi_{\min} \in [0, \pi/2), \\ \mathcal{G}_1 x + \mathcal{G}_2 y + \mathcal{G}_3 z > 0, \phi_{\min} \in (-\pi/2, 0), \\ \mathcal{G}_1 x + \mathcal{G}_2 y + \mathcal{G}_3 z < 0, \phi_{\max} \in (-\pi/2, 0), \\ \mathcal{G}_1 x + \mathcal{G}_2 y + \mathcal{G}_3 z \geq 0, \phi_{\max} \in [0, \pi/2), \\ \arccos(\boldsymbol{\varepsilon}^T \boldsymbol{\mu} / \varepsilon) \leq \pi/2, \\ \arccos(\boldsymbol{\nu}^T \boldsymbol{\zeta} / \nu) \leq \beta_r, \\ z \in (-\infty, z_m], \end{cases} \quad (18)$$

where $\boldsymbol{\zeta} = [\cos \vartheta_r \cos \alpha_r, \cos \vartheta_r \sin \alpha_r, \sin \vartheta_r]^T$ and $\boldsymbol{\nu} = [x, y, z]^T$. Referring to the reflection propagation theory [8], [18], the reflected energy $\mathcal{Q}_{r,\text{ref}}$ can be derived as

$$\mathcal{Q}_{r,\text{ref}} = \iint_{\text{ERA}} \frac{\mathcal{Q}_t (\kappa + 1) \cos^\kappa \varpi \cos \vartheta_i \cos \delta}{2\pi \varepsilon^2 \nu^2} \times \mathcal{A} v_r \Delta(\vartheta_1, \vartheta_2) \exp[-k_e(\varepsilon + \nu)] dy dz, \quad (19)$$

where ϑ_i denotes the incidence angle between $\boldsymbol{\varepsilon}$ and the normal vector $-\mathbf{n} = [-1, 0, 0]^T$ of the reflection region; v_r denotes the reflection coefficient; ϑ_1 and ϑ_2 are the angles between \mathbf{n} and $-\boldsymbol{\nu}$, and \mathbf{n} and $\boldsymbol{\varepsilon}_s$, respectively, and $\boldsymbol{\varepsilon}_s$ represents the direction vector of the specular reflection of $\boldsymbol{\varepsilon}$; and $\Delta(\vartheta_1, \vartheta_2)$ denotes the reflection pattern of the obstacle and can be given by [19]

$$\Delta(\vartheta_1, \vartheta_2) = \xi \frac{\cos \vartheta_1}{\pi} + (1 - \xi) \frac{m_s + 1}{2\pi} \cos^{m_s} \vartheta_2, \quad (20)$$

where ξ is the percentage of the incident signal that is reflected diffusely and supposes values between 0 and 1, and m_s is the directivity of the specular components.

In summary, the path loss of LED-based NLoS UV channel incorporating a cuboid-shaped obstacle can be expressed as

$$\Xi[\text{dB}] = 10 \log_{10} \frac{\mathcal{Q}_t}{\mathcal{Q}_{r,\text{sca}} + \mathcal{Q}_{r,\text{ref}}}. \quad (21)$$

V. SIMULATIONS AND EXPERIMENTAL RESULTS

The schematic diagram of NLoS UV communication systems is shown in Fig. 2. The transmitter is composed of five parts: the power supply, the modulation module, the UV LED, the rotation stage, and the heat abstractor, where the rotation stage is utilized to regulate the transceiver elevation and azimuth angles, and the heat abstractor is employed to cool the LED to ensure that it can work normally. Throughout the experiment, the power setting of the UV LED complies with the safety radiation standards [20]. The receiver is composed of six parts: the power supply, the UV photomultiplier tube (PMT) loaded with filter, the amplifier, the oscilloscope, and the photon counter. Regarding the specific

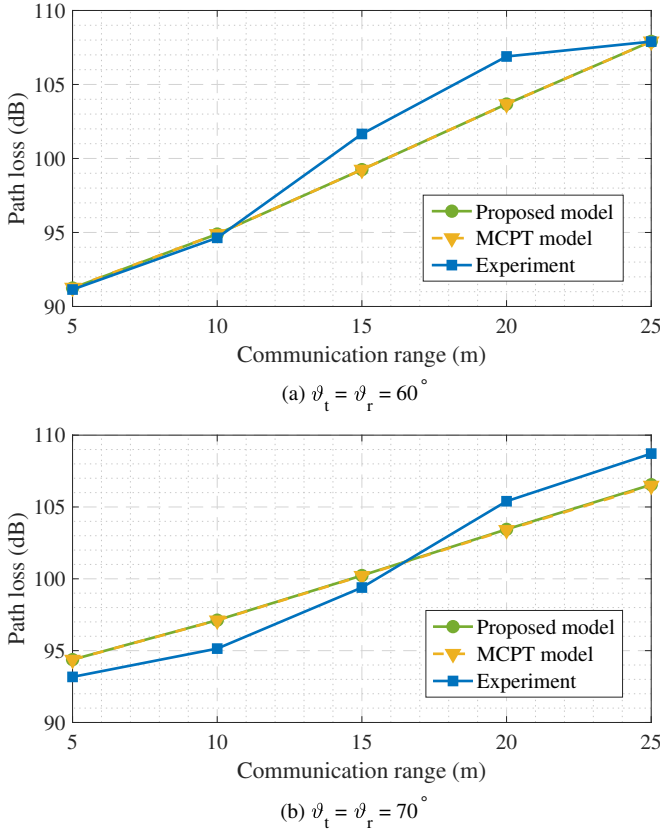


Fig. 3. Path loss results of the proposed model and the MCPT model as well as corresponding experimental results for different ϑ_t and ϑ_r values.

TABLE I
PARAMETER SETTINGS FOR VALIDATION

Parameters	Values	Parameters	Values
k_s^{Ray}	0.24 km^{-1}	$\beta_{1/2}$	$\pi/3$
k_s^{Mie}	0.25 km^{-1}	β_r	$\pi/12$
k_a	0.90 km^{-1}	α_t	$-\pi + 10^{-6}$
γ	0.017	α_r	$\pi - 10^{-6}$
g	0.72	\mathcal{A}	1.92 cm^2
f	0.5	m_s	16
v_r	0.19	ξ	0.28
x_m	-24 m	s	30 m
y_m	10 m	w	50 m
z_m	110 m	P_t	50 mW

experimental platforms, they can be found easily in our previous work [18].

We verify the proposed model by comparing it to the MCPT model [18] through simulations and experiments. Comparisons are provided in Fig. 3, and the associated parameter settings are presented in Table. I. Results show that the path loss curves of the proposed model agree well with those of the MCPT model under the identical parameter settings, while its calculation time is at least one order of magnitude lower than that of the MCPT

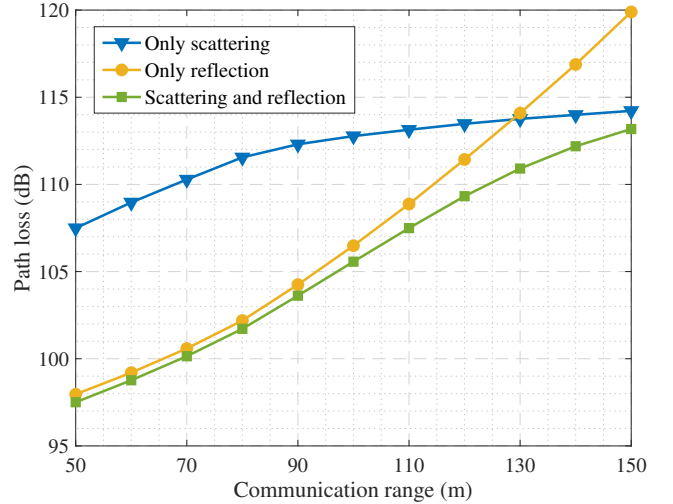


Fig. 4. Comparison of path loss for different types of received energy, namely, scattering, reflection, and both scattering and reflection.

model. Note that to be in accordance with the parameter settings in [18], the setting of y_m is inconsistent with the defined range. However, this does not influence the derivation process for the upper and lower limits of the triple integral and the factor \mathcal{S}_{wei} in the model. Taking the experimental results as the benchmark, the root-mean-square error (RMSE) is introduced to assess the accuracy of the proposed model, which can be given by [16]

$$\text{RMSE} = \sqrt{\frac{1}{\mathcal{K}} \sum_{i=1}^{\mathcal{K}} [\Xi_{\text{pro}}(x_i) - \Xi_{\text{exp}}(x_i)]^2}, \quad (22)$$

where x_i represents the i -th ($i = 1, 2, \dots, \mathcal{K}$) value of the given variable, and $\Xi_{\text{pro}}(x_i)$ and $\Xi_{\text{exp}}(x_i)$ denote the path loss of x_i obtained by the proposed model and experiments, respectively. The RMSEs of the proposed model for Figs. 3(a) and 3(b) are 1.80 dB and 1.70 dB, respectively, which demonstrates that the proposed model performs well in evaluating the channel attenuation of LED-based NLoS UV communication systems with a cuboid-shaped obstacle. Regarding the difference between the predicted data and experimental results, it is mainly caused by the unevenness of the reflection surface and the unstable value of the reflection coefficient.

Following that, we investigate the path loss for different types of received energy, as provided in Fig. 4, where the path losses for scattering and reflection are defined as $10 \log_{10}(Q_t/Q_{r,\text{sca}})$ and $10 \log_{10}(Q_t/Q_{r,\text{ref}})$, respectively. The relevant parameter settings are as follows: ϑ_t and ϑ_r are both set to 30° , α_t and α_r are set to $-7\pi/10$ and $7\pi/10$, respectively, and w , x_m , and y_m are set to 40 m, -40 m, and $r/2$, respectively. Numerical results manifest that with the given parameter settings, the contribution of reflection to the received energy is dominant when r is small, while when r is large, the contribution of scattering to the Q_r becomes dominant.

Furthermore, the influences of the obstacle's dimensions and coordinates on channel path loss are examined, as presented in

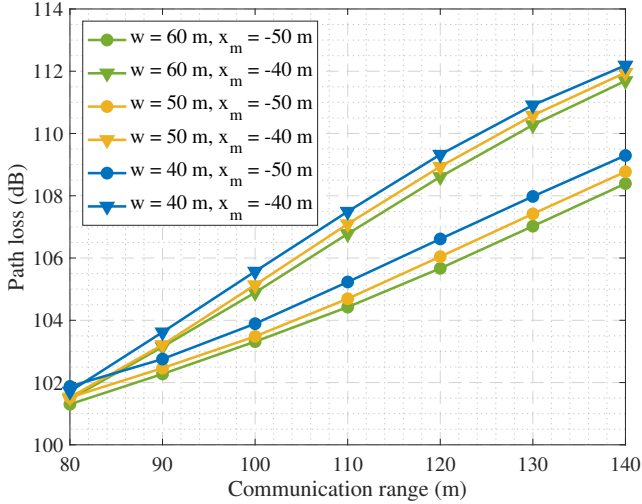


Fig. 5. Effects of obstacle's dimensions and coordinates on channel path loss.

Fig. 5. In addition to the obstacle's width w and the coordinate x_m , the remaining parameter settings are consistent with those in Fig. 4. Calculation results demonstrate that when x_m remains unchanged, increasing the obstacle's width can reduce channel path loss. For example, when x_m and r are set to -40 m and 110 m, respectively, the path losses corresponding to $w = 40$ m, 50 m, and 60 m are 107.49 dB, 107.09 dB, and 106.78 dB, respectively. The main reason for this phenomenon is that the effective reflection area is increased while increasing w . From Fig. 5, we can also discover that increasing the distance between the obstacle and the Y-axis can reduce path loss. For example, when w and r are set to 60 m and 120 m, respectively, the path losses corresponding to $x_m = -40$ m and -50 m are 108.61 dB and 105.67 dB, respectively.

Based on the above numerical results, we can conclude that to reduce channel path loss, the settings of transceiver elevation and azimuth angles, as well as the obstacle's coordinates and dimensions, should be aimed at enlarging the intersection area between the effective reflection surface and the overlap volume of the transmitter beam and receiver FoV.

VI. CONCLUSION

In this paper, we developed a channel model for NLoS UV communications incorporating a cuboid-shaped obstacle, where the radiation intensity of the LED-based light source is modeled as the Lambertian distribution. To make this model intelligible, we grouped the intersection circumstances between the receiver FoV and the obstacle into six cases, and meanwhile presented specific derivations for each case. To verify the accuracy of the proposed model, we compared it with the MCPT model through simulation results and outdoor measurements, which proved its correctness. Besides, numerical results revealed that increasing the ERA can reduce channel path loss efficiently. Therefore, in the actual communication environments, we should enlarge the intersection area between the effective reflection surface and the overlap volume of the transmitter beam and receiver FoV.

ACKNOWLEDGEMENT

This work was supported by the National Key Research and Development Program of China (2023YFE0110600), in part by the National Natural Science Foundation of China (62401433), and in part by NSF CNS-2107216, CNS-2128368, CMMI-2222810, ECCS-2302469, Toyota, and Amazon.

REFERENCES

- [1] T. Wu, T. Cao, F. Yang, J. Song, J. Cheng, and Z. Han, "Ultraviolet-based indoor wireless communications: potentials, scenarios, and trends," *IEEE Commun. Mag.*, vol. 62, no. 3, pp. 82–88, Dec. 2023.
- [2] A. Vavoulas, H. G. Sandalidis, N. D. Chatzidiamentis, Z. Xu, and G. K. Karagiannidis, "A survey on ultraviolet C-Band (UV-C) communications," *IEEE Commun. Surveys Tuts.*, vol. 21, no. 3, pp. 2111–2133, 3rd Quart., 2019.
- [3] R. Yuan and J. Ma, "Review of ultraviolet non-line-of-sight communication," *Chin. Commun.*, vol. 13, no. 6, pp. 63–75, Jun. 2016.
- [4] J. Bian, C.-X. Wang, X. Gao, X. You, and M. Zhang, "A general 3D non-stationary wireless channel model for 5G and beyond," *IEEE Trans. Wireless Commun.*, vol. 20, no. 5, pp. 3211–3224, May 2021.
- [5] G. Chen, T. Wu, F. Yang, T. Wang, J. Song, and Z. Han, "Ultraviolet-based UAV swarm communications: potentials and challenges," *IEEE Wirel. Commun.*, vol. 29, no. 5, pp. 84–90, Oct. 2022.
- [6] S. Arya and Y. H. Chung, "A comprehensive survey on optical scattering communications: current research, new trends, and future vision," *IEEE Commun. Surveys Tuts.*, vol. 26, no. 2, pp. 1446–1477, 2nd Quart., 2024.
- [7] M. R. Luetgten, J. H. Shapiro, and D. M. Reilly, "Non-line-of-sight single-scatter propagation model," *J. Opt. Soc. Amer. A, Opt. Image Sci.*, vol. 8, no. 12, pp. 1964–1972, Dec. 1991.
- [8] T. Wu, T. Cao, F. Yang, J. Song, J. Cheng, and Z. Han, "Modeling of UV diffused-LoS communication channel incorporating obstacles: an integration perspective," *IEEE Trans. Wireless Commun.*, vol. 23, no. 10, pp. 13515–13529, Oct. 2024.
- [9] T. Wu, J. Ma, P. Su, R. Yuan, and J. Cheng, "Modeling of short-range ultraviolet communication channel based on spherical coordinate system," *IEEE Commun. Lett.*, vol. 23, no. 2, pp. 242–245, Feb. 2019.
- [10] R. Yuan, J. Ma, P. Su, Y. Dong, and J. Cheng, "Monte-Carlo integration models for multiple scattering based optical wireless communication," *IEEE Trans. Commun.*, vol. 68, no. 1, pp. 334–348, Jan. 2020.
- [11] L. Liao, Z. Li, T. Lang, and G. Chen, "UV LED array based NLOS UV turbulence channel modeling and experimental verification," *Opt. Express*, vol. 23, no. 17, pp. 21825–21835, Aug. 2015.
- [12] G. Chen, Z. Xu, H. Ding, and B. M. Sadler, "Path loss modeling and performance trade-off study for short-range non-line-of-sight ultraviolet communications," *Opt. Exp.*, vol. 17, no. 5, pp. 3929–3940, Mar. 2009.
- [13] Z. Xu, H. Ding, B. M. Sadler, and G. Chen, "Analytical performance study of solar blind non-line-of-sight ultraviolet short-range communication links," *Opt. Lett.*, vol. 33, no. 16, pp. 1860–1862, Aug. 2008.
- [14] R. Yuan, J. Ma, P. Su, and Z. He, "An integral model of two-order and three-order scattering for non-line-of-sight ultraviolet communication in a narrow beam case," *IEEE Commun. Lett.*, vol. 20, no. 12, pp. 2366–2369, Dec. 2016.
- [15] T. Wu, J. Ma, R. Yuan, P. Su, and J. Cheng, "Single-scatter model for short-range ultraviolet communication in a narrow beam case," *IEEE Photonics Technol. Lett.*, vol. 31, no. 3, pp. 265–268, Feb. 2019.
- [16] T. Cao, J. Song, and C. Pan, "Simplified closed-form single-scatter path loss model of non-line-of-sight ultraviolet communications in noncoplanar geometry," *IEEE J. Quantum Electron.*, vol. 57, no. 2, pp. 1–9, Apr. 2021.
- [17] H. Zhang, H. Yin, H. Jia, J. Yang, and S. Chang, "Study of effects of obstacle on non-line-of-sight ultraviolet communication links," *Opt. Express*, vol. 19, no. 22, pp. 21216–21226, Oct. 2011.
- [18] T. Cao, X. Gao, T. Wu, C. Pan, and J. Song, "Reflection-assisted non-line-of-sight ultraviolet communications," *J. Lightwave Technol.*, vol. 40, no. 7, pp. 1953–1961, Apr. 2022.
- [19] T. Cao, T. Wu, C. Pan, and J. Song, "Single-collision-induced path loss model of reflection-assisted non-line-of-sight ultraviolet communications," *Opt. Express*, vol. 30, no. 9, pp. 15227–15237, Apr. 2022.
- [20] T. Wu, F. Yang, T. Cao, and J. Song, "Modeling of ultraviolet propagation from air to human epidermis with wavelength range of 200–300 nm," *Opt. Lett.*, vol. 47, no. 7, pp. 1662–1665, Apr. 2022.